applied sciences

MDPI

Article

Corrosion and Thermal Shock Behavior of Atmospheric Plasma Spraying Coatings on Agricultural Disc Harrows

Corneliu Munteanu [1,2], Ramona Cimpoeșu [3], Fabian-Cezar Lupu [1], Boris Nazar [4], Bogdan Istrate [1,*], Iurie Melnic [4] and Visanu Vitali [4]

[1] Mechanical Engineering, Mechatronics and Robotics Department, Mechanical Engineering Faculty, "Gheorghe Asachi" Technical University of Iasi, 700050 Iasi, Romania; corneliu.munteanu@academic.tuiasi.ro (C.M.); fabian-cezar.lupu@academic.tuiasi.ro (F.-C.L.)
[2] Technical Sciences Academy of Romania, 26 Dacia Blvd., 030167 Bucharest, Romania
[3] Materials Science Department, Faculty of Materials Science and Engineering, "Gheorghe Asachi" Technical University of Iasi, 700050 Iasi, Romania; ramona.cimpoesu@academic.tuiasi.ro
[4] Mechanical Engineering Department, Technical University of Moldova, Bd. Stefan Cel Mare 168. L, MD-2004 Chisinau, Moldova; boris.nazar@if.utm.md (B.N.); iurie.melnic@im.utm.md (I.M.); visanuvitali@gmail.com (V.V.)
* Correspondence: bogdan.istrate@academic.tuiasi.ro

Abstract

Atmospheric plasma spraying (APS) represents a critical solution for enhancing the durability of agricultural components, such as harrow discs, which are subjected to synergistic wear and corrosion during soil cultivation. This study presents experimental results evaluating the electrochemical corrosion behavior and thermal shock resistance of discs coated via atmospheric plasma thermal spraying. Both metallic and ceramic materials, in powder form, from established manufacturers were used to produce the coatings, and the three types of coatings (two metallic and one ceramic) have the following chemical compositions and trade names: $W_2C/WC12Co$ (Metco71NS), Cr_2O_3-4SiO_2-3TiO (Metco136F) and Co25.5Cr10.5Ni7.5W0.5C (Metco45C-NS). The coatings were analyzed using electron microscopy to evaluate the surfaces following corrosion testing. The ceramic coating based on the Cr_2O_3-4SiO_2-3TiO demonstrated the highest protective efficiency by increasing the charge transfer resistance from 307 Ω/cm^2 to 2213 Ω/cm^2 for the ceramic coating. It provided a superior physical barrier, reducing the corrosion current density from 0.140 mA/cm^2 for unprotected substrate to 0.004 mA/cm^2, representing an improvement of nearly two orders of magnitude. These findings demonstrate that implementing Cr_2O_3-4SiO_2-3TiO ceramic systems can significantly extend the operational lifespan of soil-engaging components, providing a cost-effective strategy for reducing maintenance intervals and material loss in aggressive agricultural environments.

Keywords: agriculture; corrosion resistance; thermal shock; thermal deposition

Check for updates

Academic Editor: Andrea Atrei

Received: 24 March 2026
Revised: 3 April 2026
Accepted: 8 April 2026
Published: 10 April 2026

1. Introduction

Agricultural machinery, particularly harrow discs, is subject to extreme operating conditions. These include abrasive wear, as well as exposure to varying levels of moisture and chemicals found in different types of soil. This makes these components prone to accelerated wear and corrosion, reducing equipment lifespan and increasing maintenance costs. Traditional solutions, such as hardened steel alloys, only offer limited protection in corrosive environments and require frequent maintenance, which affects productivity

https://doi.org/10.3390/app16083703

and can result in prolonged downtime [1–3]. The selection of low-carbon steel as the substrate material reflects the industrial standard for harrow disc manufacturing, where boron-alloyed steels and heat-treated carbon steel are predominantly used for their impact toughness. However, the service life of these components is governed by a complex hierarchy of degradation factors. While mechanical wear (abrasion) in high-silica soils is numerically the dominant cause of material loss, electrochemical corrosion acts as a critical synergistic catalyst. Corrosion pits and selective binder leaching (particularly in cermets) create localized stress concentrators and weaken the coating-substrate interface, leading to delamination and exfoliation.

An alternative solution is atmospheric plasma spraying (APS), a well-established method of depositing wear- and corrosion-resistant ceramic and metallic coatings thanks to its high deposition rate and versatile powders and parameters. The process involves propelling powders (partially or fully molten particles) into a plasma jet at temperatures exceeding 10,000 °C. The particles then impact the substrate, forming dense layers that adhere firmly to the base material. APS coatings improve mechanical adhesion and resistance to multiple stresses, as well as corrosion resistance. This makes them suitable for use in aggressive environments, such as on agricultural plough discs, which are subjected to extreme conditions during soil cultivation [4–6].

Electrochemical corrosion is a major form of degradation for components exposed to moist soil and is accelerated by fluctuations in pH and mineral salts. Recent studies show that APS coatings containing nickel, chromium or ceramic compounds can significantly reduce corrosion rates due to surface passivation; however, defects such as pores can initiate pitting corrosion. In an agricultural context, these coatings can extend the service life of machine components by 2–3 times compared to unprotected substrates. The literature highlights the advantages of APS deposition technology over similar methods, such as HVOF, for certain applications due to its low porosity and resistance to electrochemical corrosion. However, few studies address specific agricultural applications such as harrow discs, where the combination of corrosion and thermal shock is critical for maximising service life [7–9].

In this study, three types of powders (metallic and ceramic) were used for thermal coatings and layer characterization. These powders have the following chemical compositions and trade names: W_2C/WC-12Co (Metco 71NS, abrasion-resistant metallic powder), Cr_2O_3-4SiO_2-3TiO (Metco 136F, ceramic powder with thermal protection properties), and Co25.5Cr10.5Ni7.5W0.5C (Metco 45C-NS, powder with high anti-corrosion properties). These powders form hard layers exceeding 1000 HV with high resistance to corrosion and thermal shock, thereby improving performance under combined wear and corrosion conditions during soil processing. Thermal shocks occur during equipment operation due to rapid temperature changes (e.g., contact with hot soil or sudden cooling), generating residual stresses and microcracks. APS ceramic coatings, such as those based on Cr_2O_3, demonstrate superior resistance due to low thermal conductivity and improved toughness through alloying with TiO_2. Several studies indicate that the dense structures obtained via APS reduce delamination under thermal cycling, unlike those produced by other conventional methods [10–12].

Atmospheric plasma spraying (APS) coatings have been widely investigated for their ability to enhance wear and corrosion resistance in aggressive environments, with numerous studies demonstrating their effectiveness in reducing material degradation through the formation of dense lamellar structures and chemically stable surface layers. In the context of agricultural applications, existing research has predominantly focused on abrasive wear mechanisms, tribological behaviour, and field performance of coated components under soil interaction conditions [13,14]. In parallel, corrosion studies on thermal spray coatings have largely been conducted under controlled laboratory conditions, typically without considering prior thermal or mechanical degradation of the coating system [15].

However, real operating conditions for soil-engaging tools involve complex and coupled degradation mechanisms, including not only abrasion and corrosion but also transient thermal loading, generated by frictional heating, dry soil interaction, or accidental exposure to elevated temperatures followed by rapid cooling. Despite the recognized sensitivity of APS coatings to thermal stresses—due to their lamellar structure, residual stresses, and inherent porosity—the influence of thermal shock on subsequent electrochemical behaviour and corrosion resistance remains insufficiently addressed in the literature [16]. While Atmospheric Plasma Spraying (APS) is established in aerospace, its application for enhancing agricultural harrow discs against synergistic soil abrasion and corrosion remains under-explored. This study fills this gap by providing a mechanistic comparison between three types of coatings. Utilizing EIS to decode interfacial kinetics, the work identifies the 'near-ideal dielectric barrier' of Cr_2O_3-4SiO_2-3TiO system and deciphers the selective binder leaching in cermets. Ultimately, this research establishes a quantitative framework for developing high-performance, corrosion-resistant coatings optimized for extreme soil-cultivation environments.

Current studies rarely investigate how rapid heating–cooling cycles modify coating integrity, microcrack formation, or interlamellar cohesion, and how these changes affect electrolyte penetration and corrosion kinetics. Consequently, there is a lack of systematic data linking thermal shock-induced microstructural damage with electrochemical performance degradation.

The present study addresses this gap by providing an integrated evaluation of APS coatings subjected to severe thermal shock conditions, followed by detailed electrochemical characterization. By comparing corrosion behaviour before and after thermal cycling, this work offers new insights into the stability of protective mechanisms in realistic service conditions, where thermal, mechanical, and chemical factors act simultaneously.

This paper presents experimental results evaluating the electrochemical corrosion and thermal shock resistance of APS coatings deposited on agricultural plough discs using three types of coating. The microstructural properties of the coating surfaces were characterised using scanning electron microscopy (SEM/EDS), providing new data for optimising the performance of agricultural machinery used for soil preparation.

2. Materials and Methods

The experimental study was conducted on a low-carbon steel substrate and evaluated in both its uncoated (initial) state and after the deposition of three distinct thermal spray coatings (Samples 1, 2 and 3) using specific Metco powders. Coated samples were obtained with three different compositions, as follows: (i) Sample 1—Metco 71NS, (ii) Sample 2—Metco 136F, and (iii) Sample 3—Metco 45C-NS (Co 25.5Cr 10.5Ni 7.5W 0.5C). The detailed chemical compositions and physical characteristics of the three investigated coatings are summarized in Table 1.

Thermal plasma spray coatings were applied to the experimental samples using the SPRAYWIZARD-9MCE system (Sulzer Metco, Westbury, NY, USA). To ensure optimal adhesion of the coating to the substrate, the samples were sandblasted and degreased prior to coating. The deposition system comprises several related pieces of equipment [13] such as gas dispensers (for Ar, He, N_2 and H_2) and powder dispensers, which form the plasma jet and transport the powder (the raw material) to the deposition gun. It also includes a rotating table, which allows the sample to rotate relative to the movement of the gun during deposition. Figure 1 schematically illustrates the work stages, starting with the formation of thermal deposits and sample preparation, through to the experimental tests to determine corrosion behavior, thermal shock tests, and microstructural analysis.

Table 1. Main characteristics and nominal compositions of the thermal spray powders.

Coating Designation	Trade Name (Metco)	Nominal Composition	Particle Size Range (µm)	Key Properties/Characteristics
Sample 1	Metco 71NS	W_2C/WC 12Co	−90 + 53	High hardness Superior abrasive wear resistance.
Sample 2	Metco 136F	Cr_2O_3 $4SiO_2$ $4TiO_3$	−63 + 5	Abrasion Protection, Impact Resistance
Sample 3	Metco 45C-NS	Co 25.5Cr 10.5Ni 7.5W 0.5C	−75 + 45	Solid Particle Erosion Protection, Dimensional Restoration, Abrasion Protection

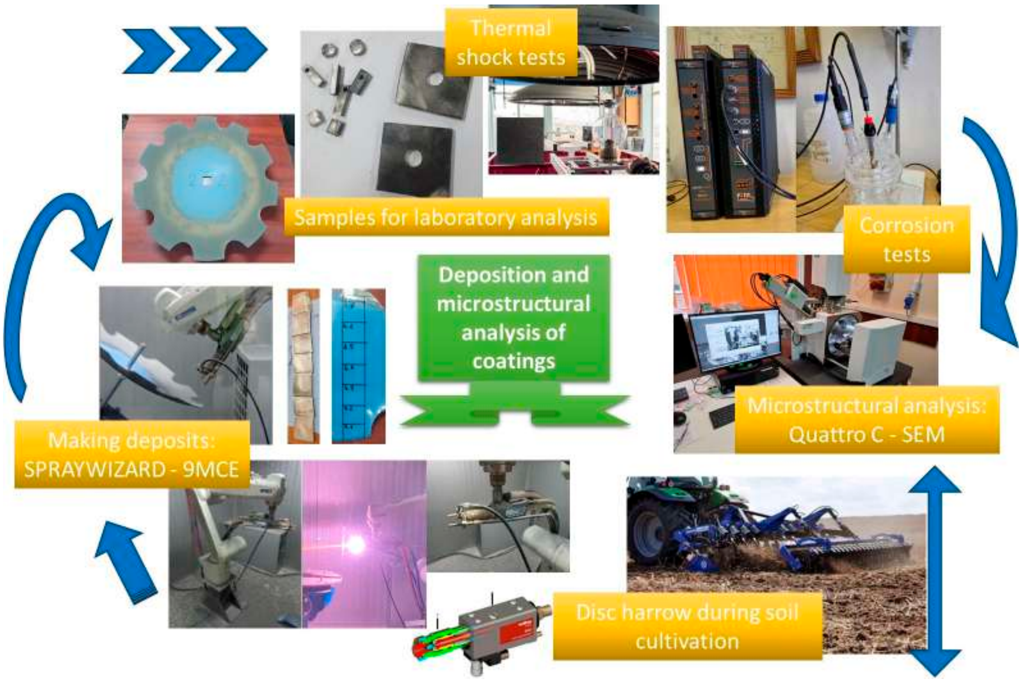

Figure 1. Schematic diagram of the deposition process and experimental analysis procedures.

Microstructural property analyses were performed using a Thermo Fisher FEG Quattro C 2024 scanning electron microscope (SEM/EDS), manufactured in the Brno, Czech Republic. The samples were prepared for analysis by being cut using a Metacut 302 machine (Metkon, Bursa, Turkey) and embedded in resin using a Metkon Eco-Press 52 machine (Metkon, Bursa, Turkey).

All electrochemical investigations were performed in a standard three-electrode configuration using an OrigaStat potentiostat/galvanostat (manufactured by OrigaLys ElecTroChem SAS, Rhône, France) controlled by OrigaMaster 5 software, to evaluate the anticorrosive performance of the deposited layers relative to the reference steel substrate. The samples served as the working electrode and were mounted to expose a constant active surface area of 0.6 cm^2 to the corrosive environment represented by a 0.9% NaCl solution. The reference potential was monitored using a saturated calomel electrode (SCE) and the electrical circuit was closed using a platinum counter electrode [17]. The experimental protocol began with the open-circuit potential (OCP) being monitored for 30 min—the time required for thermodynamic equilibrium to be reached at the layer-electrolyte interface. Once stabilised, electrochemical impedance spectroscopy (EIS) analysis was performed by applying a low-amplitude sinusoidal signal (10 mV) within a frequency range of 100 kHz to 10 mHz. For potentiodynamic polarisation, the scan was performed from −250 mV vs. OCP to +250 mV vs. OCP at a scan rate of 1 mV/s. The resulting data were processed using Tafel extrapolation, enabling the corrosion current density (icor) and the specific degradation rate for each coating system to be determined in comparison to the initial steel specimen. To investigate the kinetics of corrosion processes and the susceptibility of materials to localised degradation phenomena, cyclic linear polarisation tests were performed [18]. The potential scan was carried out at a constant rate of 5 mV/s, starting from the cathodic region and advancing towards positive anodic values. This was followed by a reversal of the scan direction. The impedance data were modelled using ZView software v. 3.22 and the EIS spectra were interpreted based on equivalent electrical circuits adapted to the complexity of the layer interface. To ensure reproducibility and validation of the results, all electrochemical tests were performed three times at a constant temperature of 25 °C.

The thermal shock tests were conducted at the PROMES-CNRS facility in Font-Romeu, France, utilizing a high-flux solar furnace. The experimental configuration consists of the following key components: For solar collection and concentration a primary heliostat (tracking mirror system) collects solar radiation and reflects it toward a 2 m diameter solar concentrator. This system is designed to achieve extremely high temperatures within seconds, simulating severe thermal shock conditions. The samples (steel base with ceramic coatings) were mounted on a specialized metal support. To protect the structural integrity of the fixture, the support was continuously water-cooled. The motion control was realized by putting the entire assembly on a mobile trolley. This allowed for the rapid introduction and extraction of samples into the solar focal point, enabling precise control over the heating cycles and maintenance periods. Two cooling regimes were implemented to evaluate different thermal gradients: natural air cooling and forced cooling using compressed air. Temperature variations were recorded in real-time using a Graphtec data logger (Graphtec Corporation, Yokohama, Japan) connected to two thermocouples, one under the metallic substrate and the other on the ceramic surface capturing the rapid heating and cooling phases. To ensure the protection of human resources, all tests followed established safety laws, with the specific goal of neutralizing hazards that could have arisen during the experimental phases [19].

3. Results

Previous investigations on similar APS coatings applied to agricultural harrow discs indicate that the deposited layers exhibit a characteristic lamellar microstructure, typical for plasma-sprayed materials, with thicknesses ranging between approximately 220 and 320 µm depending on the coating composition. Specifically, ceramic Cr_2O_3–SiO_2–TiO_2 coatings present thickness values of about 220–260 µm, while carbide (WC/W_2C–Co) and Co-based alloy coatings reach slightly higher values of 280–320 µm and 250–290 µm, respectively [14]. Microstructural analysis further reveals relatively low porosity levels, generally below 5% for ceramic and Co-based coatings, indicating dense and well-adhered layers, whereas carbide coatings tend to exhibit locally increased porosity and microcrack density, particularly at carbide–binder interfaces. This structural heterogeneity is consistent with the intrinsic nature of APS deposition, where rapid solidification of molten particles leads to splat-based morphology and interlamellar boundaries [14]. Although detailed roughness values are not always explicitly quantified, the literature consistently describes APS coatings as having relatively high surface roughness due to partially melted particles and splat stacking, which contributes to mechanical interlocking but may also facilitate electrolyte penetration in more porous systems. These microstructural features play a critical role in determining both corrosion resistance and thermomechanical stability under service conditions.

3.1. Electrochemical Characterization

The results obtained through potentiodynamic polarization, Figure 2a,b provide an initial quantitative insight into corrosion kinetics, highlighting the clear contrast between unprotected steel substrates and advanced coating systems. The Tafel curves, Figure 2a, recorded for the four samples indicate a significant shift in corrosion potential (E_{corr}) towards more noble (more positive) values for the coated samples [15,20]. This suggests a reduction in anodic activity at the metal-electrolyte interface.

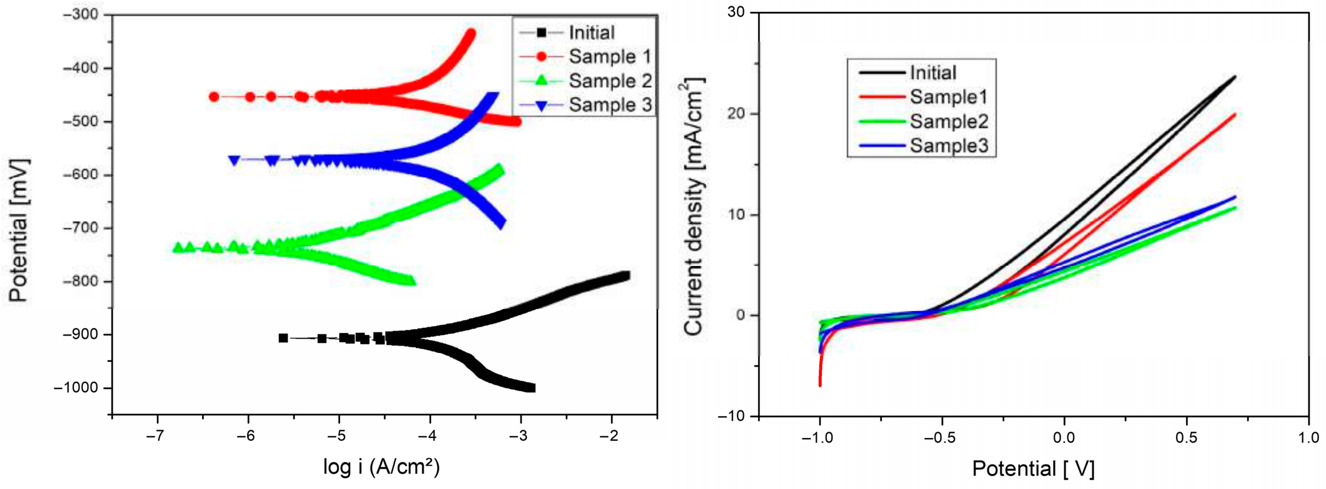

(**a**) (**b**)

Figure 2. Electrochemical results in 0.9% NaCl for the initial substrate and S1–S3 coatings: (**a**) potentiodynamic polarisation (Tafel) and (**b**) cyclic polarisation curves.

Analysis of the open-circuit corrosion potential (E(I = 0)) reveals a change in the thermodynamic state of the surfaces when protective coatings are applied. For the control sample (Initial), the strongly negative value of −906 mV indicates intense chemical activity and the steel's high natural tendency to oxidize in the test environment. This value represents the reference state of the vulnerable substrate, where the absence of a barrier leads to immediate corrosion.

Analysis of the electrochemical parameters, Table 2, represented by the corrosion current density (j_{corr}) and corrosion rate (v_{corr}), confirms the effectiveness of the protective coatings in inhibiting steel degradation. While the control sample exhibits a high corrosion rate of 1.61 mm/year, corresponding to a current of 0.14 mA/cm^2, the application of Metco coating solutions systematically reduces these indicators, demonstrating their ability to act as physical and electrochemical barriers. The most significant change occurs in Sample 2 (Metco 136F), where the corrosion current density decreases by two orders of magnitude to a minimum value of 0.0045 mA/cm^2. This reduction in reaction kinetics results in a corrosion rate of just 0.054 mm/year, providing protection compared to the initial substrate. This exceptional resistance of the Cr_2O_3-4SiO_2-3TiO oxide layer can be attributed to the high structural density and chemical inertness of the ceramic phases [20]. These effectively block the penetration of chloride ions towards the steel interface, thereby limiting the formation of anodic areas.

Table 2. The electrochemical parameters obtained from Tafel extrapolation for the Initial and S1–S3 samples in 0.9% NaCl solution.

Sample	E(I = 0) (mV)	j_{corr} (mA/cm^2)	Rp (ohm/cm^2)	v_{corr} (mm/year)
Initial	−906	0.140	119.51	1.61
Sample1	−453	0.091	257.89	1.05
Sample 2	−737	0.004	2810	0.054
Sample 3	−570	0.103	248.14	1.19

For the steel control sample, the corrosion current density (j_{corr}) exhibits the highest values, reflecting an increased susceptibility to anodic dissolution in the presence of chloride ions. In contrast, analysis of the anodic and cathodic branches of Sample 1 (Metco 71NS) reveals the influence of the cobalt binder phase on the corrosion process. Although the carbide matrix (W_2C/WC) acts as a robust physical barrier, corrosion kinetics are controlled by diffusion of corrosive species through microporosities inherent in the structure. Sample 2 (Metco 136F) exhibited the most stable behaviour, where the ceramic nature of the Cr_2O_3-4SiO_2-3TiO layer induced superior resistance. The polarization curve for Sample 2 exhibits an extended passivation region, indicating that the oxide layer limits electron flow and inhibits the formation of unstable corrosion products. Meanwhile, Sample 3 (Metco 45C-NS) exhibits a smoother anodic Tafel slope than the reference steel, suggesting that the presence of chromium and nickel in the cobalt-based alloy promotes the formation of a self-healing protective film that reduces the corrosion rate by blocking active sites. By comparison, samples 1 and 3 provide moderate protection, with corrosion rates of 1.05 mm/year and 1.195 mm/year, respectively.

The electrochemical behaviour and barrier properties of the deposited layers were then investigated using electrochemical impedance spectroscopy (EIS) [21,22]. The resulting Nyquist and Bode plots are shown in Figure 3. The graphical representation of complex impedance (Figure 3a) reveals differences by an order of magnitude in the corrosion mechanisms of the four samples. All spectra are characterized by the presence of a single capacitive arc (impedance loop) in the high- and mid-frequency ranges, which suggests that the corrosion process is predominantly controlled by a single charge-transfer mechanism at the interface. The impedance spectra were modelled using the equivalent electrical circuit, Figure 3c, which allowed the contributions of each layer to the overall corrosion process to be identified. The resulting values, Table 3, confirm a systematic improvement in protective performance for all deposited systems, although there are notable variations due to the specific chemistry of the Metco powders.

Although Samples 1 and 3 exhibit a slight increase in impedance compared to the control sample, their arcs remain confined to the low-value range (below 1000 Ω/cm^2 on the real axis Zr). This behaviour suggests that, while the Co alloy layers offer some protection, the electrolyte still manages to penetrate their structure, probably via the network of micropores or the metallic binder phase [23]. This limits the system's overall resistance. The graph is defined by the capacitive arc of Sample 2, which increases considerably to values in excess of 2500 Ω/cm^2. This significant increase in the diameter of the semicircle is an indication of exceptional corrosion resistance. The arc's failure to close on the real axis demonstrates that the ceramic coating (Metco 136F) functions as an almost ideal barrier, creating a dense dielectric that decouples the substrate from the corrosive environment.

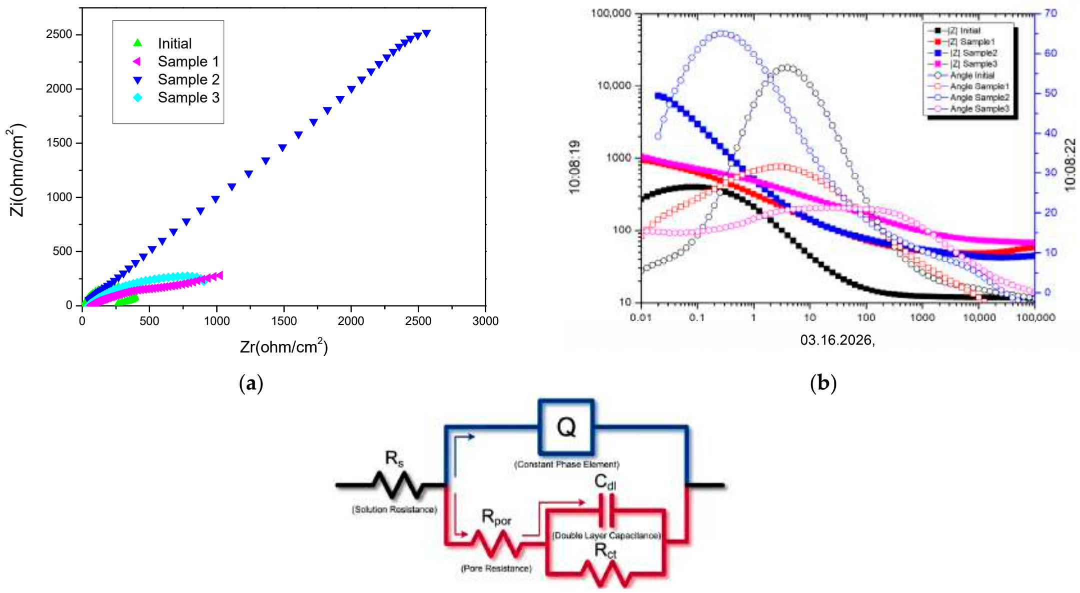

(**a**) (**b**)

(**c**)

Figure 3. EIS spectra in 0.9% NaCl: (**a**) Nyquist and (**b**) Bode plots for the initial substrate and S1–S3 coatings, (**c**) equivalent electrical circuit model R(Q(R(CR))).

Table 3. Electrochemical impedance spectroscopy (EIS) parameters obtained by fitting the experimental data with the R(Q(R(CR))) equivalent electrical circuit for the initial substrate and Metco-coated samples in aerated 0.9% NaCl solution.

Sample	**R_s Ω/cm^2**	**CPE**		**R_{por} Ω/cm^2**	**C_{dl} F/cm^2**	**R_{ct} Ω/cm^2**
		Q Ss^n/cm^2	**n**			
Initial	31	0.0006698	0.83	83	1.607×10^{-4}	307
Sample 1	50	0.001327	0.54	240	1.967×10^{-5}	1328
Sample 2	42	0.0002558	0.64	415	2.939×10^{-5}	2213
Sample 3	59	0.00089295	0.58	229	5.7×10^{-5}	881

The values for R_s show minimal variation between 31 Ω/cm^2 (Initial) and 59 Ω/cm^2 (Sample 3). This is mainly due to the conductivity of the electrolyte (0.9% NaCl) and the cell geometry being the primary factors in determining this parameter. Regarding Constant Phase Element (CPE), the parameter Q reflects the magnitude of the CPE, and the exponent n reflects the integrity and homogeneity of the surface. Sample 2 exhibits the lowest value of Q (0.558×10^{-4} Ss^n/cm^2), indicating a denser and less permeable layer. The exponent n decreases from 0.83 (base steel) to values ranging from 0.54 to 0.64 for the Metco coatings. This decrease is a typical signature of the thermal spraying process, indicating high structural heterogeneity and pronounced microscopic roughness. R_{por} measures the layer's resistance to electrolyte penetration through the pores and defects in the structure. An increase is observed from 83 Ω/cm^2 (initial) to 415 Ω/cm^2 for Sample 2. The maximum value observed for the ceramic system (Cr_2O_3-4SiO_2-3TiO) indicates that it offers the most effective physical barrier, thereby limiting chloride ion pathways to the substrate. Sample 1 and Sample 3 exhibit intermediate values of 240 and 229 Ω/cm^2, respectively, indicating a more permeable structure characteristic of metallic deposits, where secondary phases can create microchannels at the particle boundaries. It is well known that a decrease in C_{dl} suggests either an increase in the thickness of the protective film or a reduction in the area of the surface exposed to corrosion. Samples 1,2 and 3 (with values of 1.967×10^{-5}; 2.939×10^{-5}; 5.7×10^{-5}, respectively) exhibit values that are an order of magnitude lower than those of the original steel. This decrease in capacitance indicates that the metal surface is effectively shielded by a robust dielectric barrier, which minimises charge accumulation at the interface. Charge transfer resistance (Rct) is the defining parameter for corrosion rate. With an Rct of 2213 Ω/cm^2, Sample 2 is the most effective, showing an increase compared to the reference steel with an Rct of 307 Ω/cm^2. This validates the chemical superiority of the oxide system, which inhibits redox reactions at the interface much more effectively than metallic systems manage to do. Sample 1 (1328 Ω/cm^2) offers superior protection to Sample 3 (881 Ω/cm^2), suggesting that the tungsten carbide mixture (W_2C/WC) is more stable in a saline environment than the complex cobalt-chromium-nickel alloy in Sample 3 [24].

3.2. Microstructural and Chemical Characterization

Figure 4 shows the surface morphologies of the initial substrate and the three Metco-coated samples, as determined by SEM analysis after corrosion exposure in a 0.9% NaCl solution. In the initial sample, the surface is completely affected by corrosion (see Figure 4a). A granular, porous layer of corrosion products with a typical iron oxide and hydroxide appearance, based on comparative morphological studies [25]. Most notably, a network of deep microcracks traverses the surface, indicating the natural oxide layer has become structurally unstable. This morphology is characteristic of uniform and aggressive corrosion. In the absence of any protective barrier, the electrolyte is able to attack the metal substrate directly. These deep cracks act as microchannels, accelerating the diffusion of chloride ions into the steel. This phenomenon is directly correlated with the minimum charge transfer resistance (Rct = 307 $\Omega\cdot\text{cm}^2$) obtained through EIS.

The surface of the ceramic layer appears to be intact, dense and homogeneous (see Figure 4c). There are no indications of corrosion products or microcracks on the surface. An isolated agglomerate can be observed, which is likely a secondary phase intrinsic to the spraying process. There are no signs of corrosion attack. This micrograph confirms the status of the oxide system (Cr_2O_3-SiO_2-TiO_3) as a barrier. The fact that the surface has remained intact validates the hypothesis of the ceramic's superior chemical inertness and the high compactness of the layer. In samples 1 and 3, the surface is rough, with a clearly defined granular texture. Although there is no significant destruction of the reference steel, a large number of micro-pits (microscopic pitting) and a fine accumulation of particulate corrosion products are observed [26]. The hard carbide particles appear prominent, while the spaces between them appear deepened. This morphology is a classic example of selective binder leaching. The metallic cobalt, which holds the carbides together, has been anodically dissolved, leaving the carbide structure unprotected.

Figure 5 shows the characteristic energy dispersive spectroscopy (EDS) spectra of the elements identified on the surface of the samples following corrosion resistance tests, highlighting the differences caused by the nature of the coatings. In the case of the initial S4 sample, without a coating (Figure 5a), the spectrum is dominated by iron, accompanied by a low oxygen content ($\approx$7.7 at.%), which indicates limited formation of corrosion products and the absence of an effective protective layer. For sample S1 (Figure 5b), coated with Metco 71NS (W_2C/WC–12Co), a significant increase in oxygen intensity ($\approx$53 at.%) is observed, along with the pronounced presence of W and Co, suggesting marked surface oxidation and the exposure of phases characteristic of the coating, without the formation of a compact protective layer. In the case of sample S2 (Figure 4c), coated with Metco 136F (Cr_2O_3–$4SiO_2$–$4TiO_3$), the spectrum indicates a moderate oxygen content ($\approx$28 at.%) and the presence of chromium, an element essential for passivation, which confirms the formation of a stable and adherent oxide layer responsible for the superior corrosion behavior.

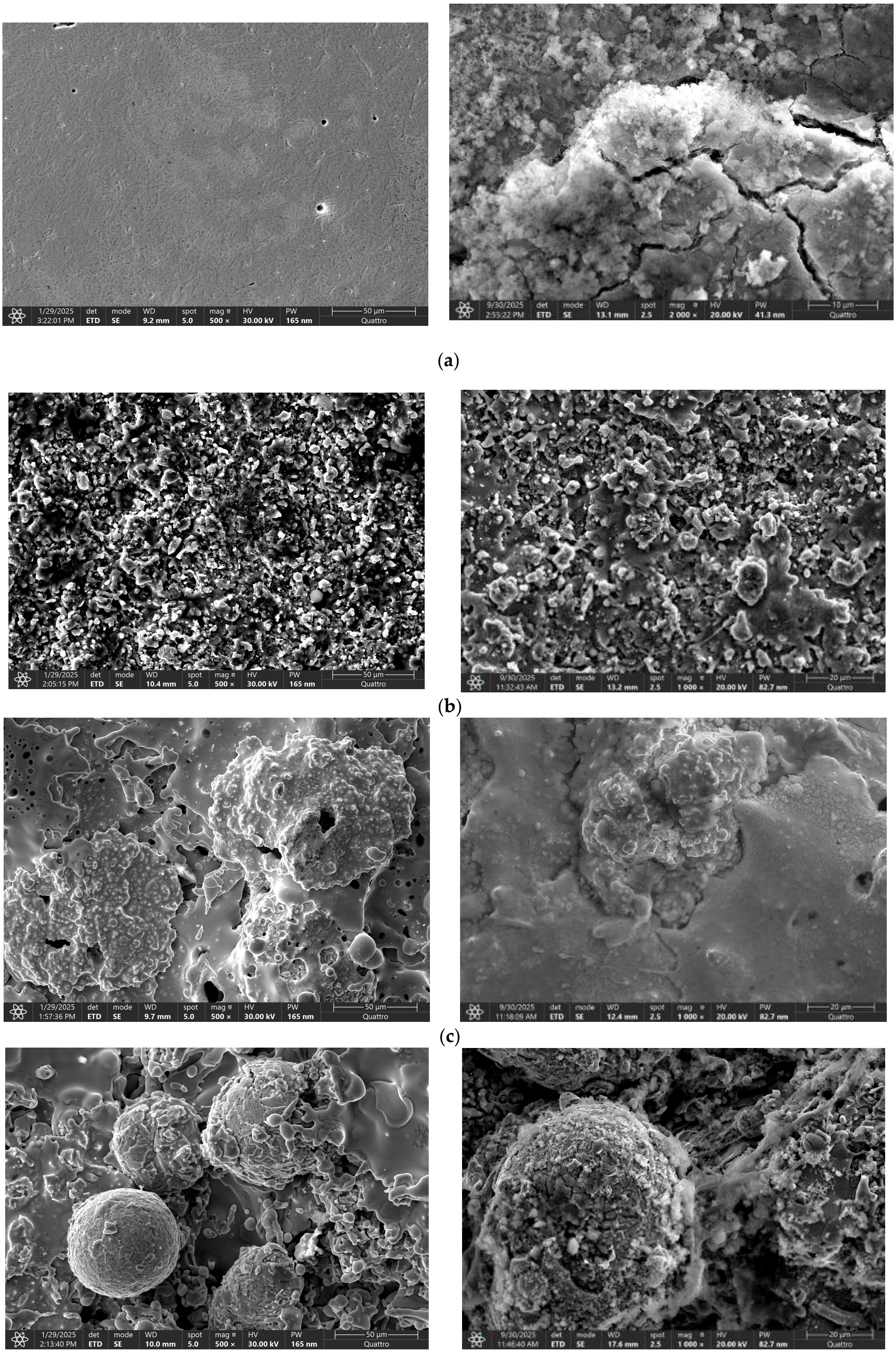

(**a**)

(**b**)

(**c**)

(**d**)

Figure 4. SEM analysis of surface before and after corrosion resistance tests: (**a**) Initial sample, (**b**) Sample 1, (**c**) Sample 2, (**d**) Sample 3.

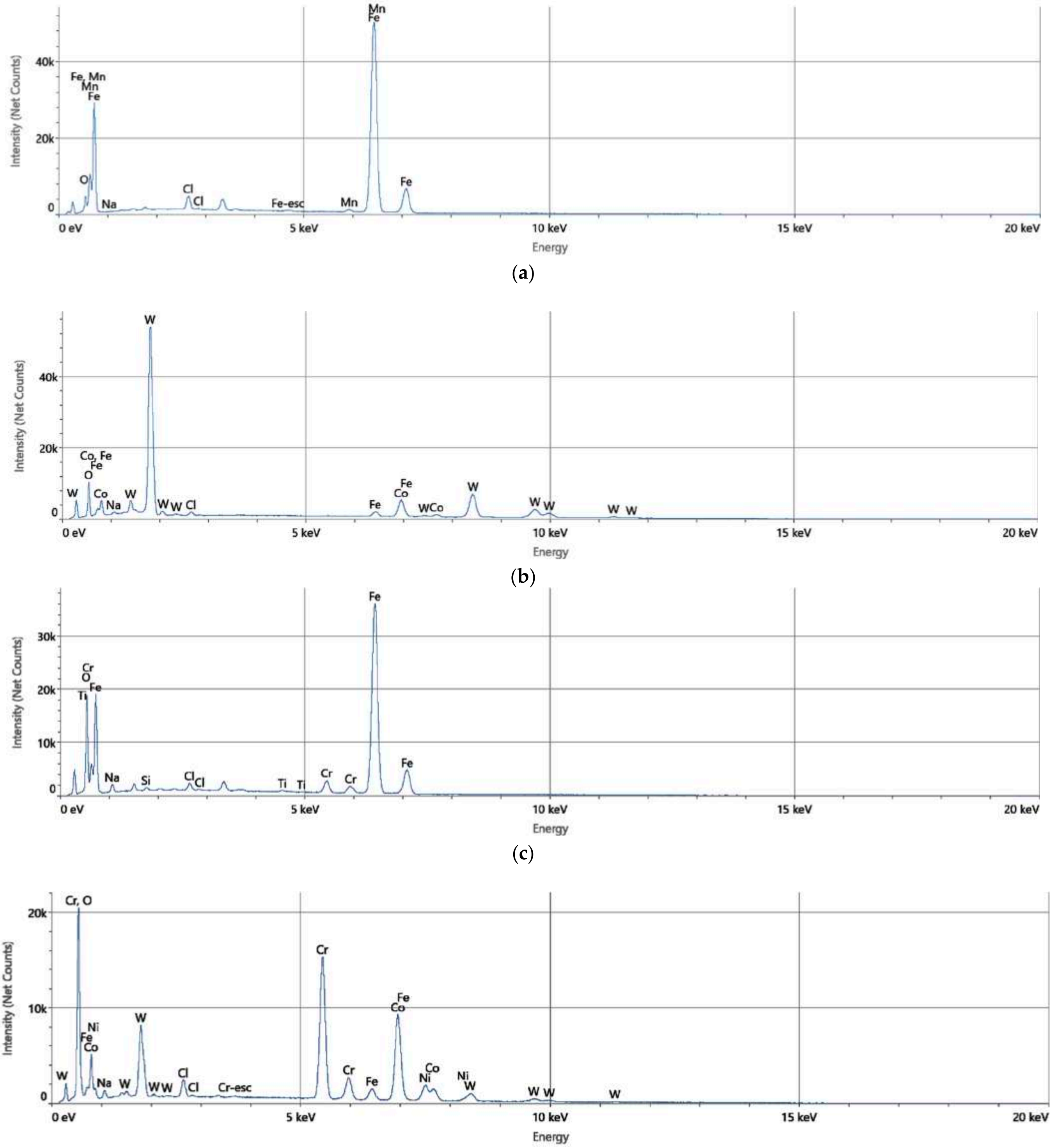

(**a**)

(**b**)

(**c**)

(**d**)

Figure 5. Energy spectrum of the elements identified on the surface (**a**) initial sample, (**b**) sample S1, (**c**) sample S2 and (**d**) sample S3.

For sample S3 (Figure 5d), coated with Metco 45C-NS (Co–Cr–Ni–W), a high oxygen content (≈48 at.%) is again observed, along with signals corresponding to the alloying elements, indicating an advanced oxidation process and less effective protection compared to S2. Overall, the spectral analysis confirms that corrosion performance is determined by the coating's ability to form a stable passive layer, with the chromium oxide-based coating (P2) being the most effective. Table 4 highlights the influence of coating composition on the degree of surface oxidation following corrosion testing. Sample S1, coated with Metco 71NS (W_2C/WC–12Co), exhibits a very high oxygen content (53.1 at.%), indicating significant oxidation, while the presence of W and Co confirms the preservation of the coating-specific phases on the surface. Sample S2, coated with Metco 136F (Cr_2O_3–$4SiO_2$–$4TiO_3$), exhibits the lowest degree of oxidation among the coated samples and the best electrochemical behavior, which can be attributed to the protective role of the chromium oxide-rich ceramic layer. In the case of sample S3, coated with Metco 45C-NS (Co–25.5Cr–10.5Ni–7.5W), the high oxygen content (48.0 at.%) indicates an advanced oxidation process, even though the presence of Cr and Ni suggests a certain tendency toward passivation. In comparison, the initial P4 sample, dominated by Fe, remains the most vulnerable to corrosion attack. Overall, the results confirm that the Metco 136F coating provides the most effective corrosion protection.

Table 4. Chemical composition on the surfaces of the samples after corrosion resistance test.

Element	Initial At.%	Init. Wt.%	Init. Err At.%	Init. Err Wt.%	S1 At.%	S1 Wt.%	Err At.%	Err Wt.%	S2 At.%	S2 Wt.%	Err At.%	Err Wt.%	S3 At.%	S3 Wt.%	Err At.%	Err Wt.%
O	7.7	2.3	0.1	0.0	53.1	12.0	0.5	0.1	28.3	10.5	0.2	0.1	48.0	19.6	0.3	0.1
Na	0.0	0.0	—	—	0.9	0.3	0.1	0.0	3.6	1.9	0.1	0.0	1.7	1.0	0.1	0.0
Si									0.3	0.2	0.0	0.0				
Cl	2.6	1.7	0.0	0.0	1.6	0.8	0.1	0.0	0.9	0.8	0.0	0.0	1.5	1.3	0.0	0.0
Ti									0.1	0.2	0.0	0.0				
Cr									2.6	3.1	0.0	0.0	20.1	26.7	0.1	0.1
Mn	1.6	1.7	0.1	0.1												
Fe	88.1	94.3	0.2	0.2	3.3	2.6	0.1	0.1	64.2	83.3	0.2	0.2	2.7	3.8	0.1	0.1
Co					12.7	10.6	0.1	0.1					19.8	29.6	0.1	0.2
Ni													3.4	5.1	0.1	0.1
W					28.4	73.7	0.2	0.6					2.8	12.9	0.1	0.4

St dev. (from five determinations): O: ±0.75; Na: ±0.05; Si: ±0.05; Cl: ±0.05; Ti: ±0.05; Cr: ±0.12; Mn: ±0.9; Fe: ±0.3; Co: ±0.15; Ni: ±0.1 and W: ±0.1.

Figure 6 shows the spatial distributions of the elements on the surface of the samples following the corrosion resistance tests, providing information on the uniformity and the degradation mechanism. In the case of the initial S4 sample, the distribution of iron is predominant and relatively uniform, while oxygen appears localized, confirming limited and uneven surface oxidation. This distribution indicates the absence of a continuous protective layer. For sample S1, the distributions reveal a significant and uneven accumulation of oxygen, associated with regions rich in W and Co. This heterogeneity suggests the formation of discontinuous corrosion products and the presence of active zones where corrosion is more intense.

In the case of sample S2, the elemental distributions are much more uniform, particularly for oxygen and chromium. This correlation indicates the formation of a continuous, compact, and adherent oxide layer, characteristic of effective passivation. The uniform distribution of this layer explains the high corrosion resistance observed electrochemically. For sample P3, the distributions show an uneven distribution of oxygen, correlated with areas where alloying elements (Co, Cr, Ni, and W) are concentrated. This distribution suggests a localized corrosion mechanism and limited effectiveness of the formed passive layer. In conclusion, the analysis of the elemental distributions confirms that corrosion resistance is closely linked to the coating's ability to generate a uniform and protective oxide layer, a condition optimally met by the Metco 136F coating (Sample 2).

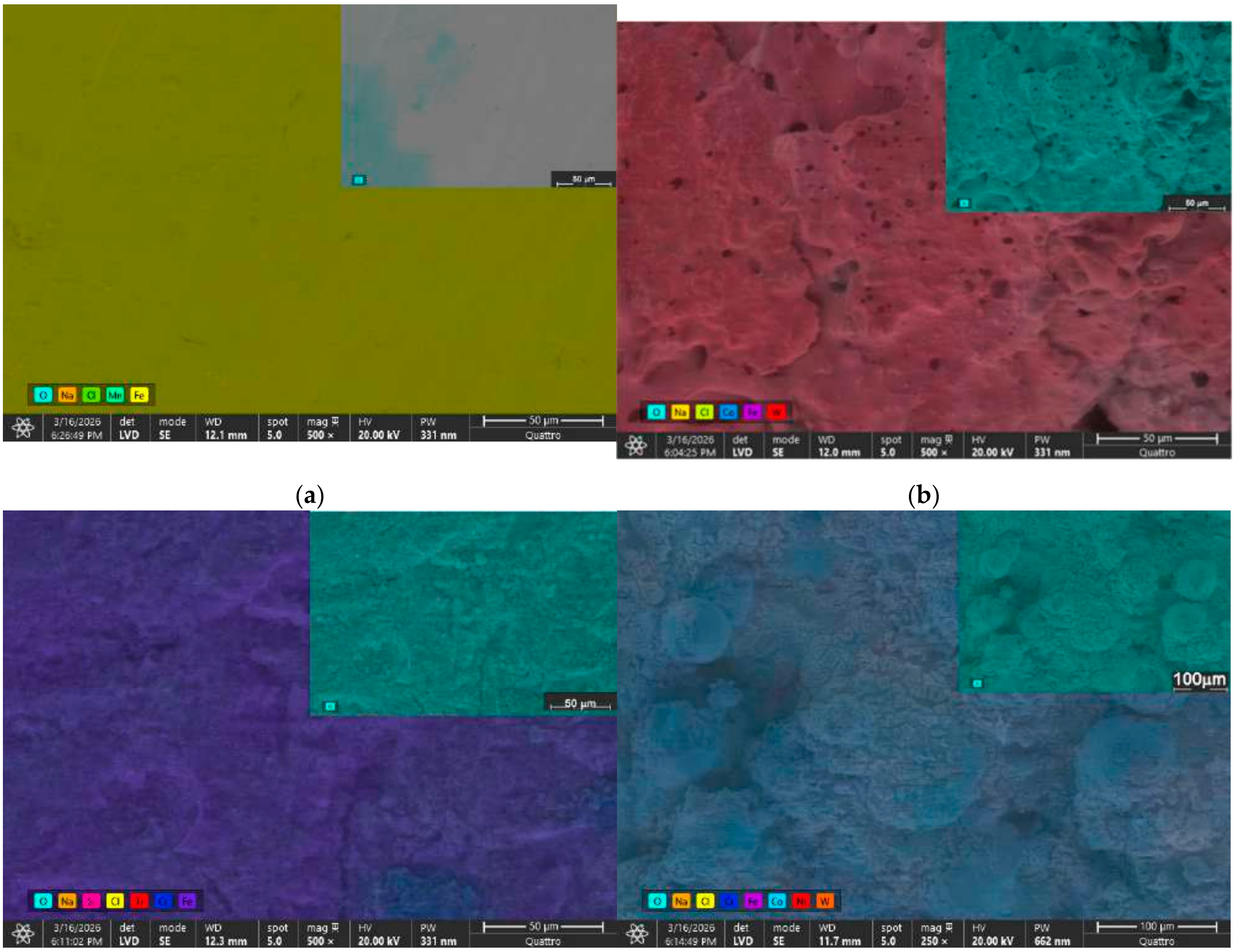

(**a**) (**b**)

(**c**) (**d**)

Figure 6. Elemental distributions of the elements identified on the surfaces of the samples after corrosion resistance tests: (**a**) initial, (**b**) S1, (**c**) S2 and (**d**) S3.

3.3. Thermal Shock Characterization

Analysis of the experimental data for the four samples highlights the setup's high capability to generate steep temperature gradients and maintain the target temperature. The temperature of 800 °C was reached and maintained with high precision; all samples reached and exceeded the 800 °C threshold during the heating cycles, Figure 7. For example, Sample 1 reached temperatures of approximately 860–870 °C, while Sample 2 recorded peaks of over 890 °C. The holding period at the plateau temperature (approx. 800 °C) was 10 s, in accordance with the described methodology. The data show that the solar flux was kept constant during this interval before the sample was removed for cooling. Based on the heating and cooling rates (metal + ceramic layer assembly) from the analysis of the data files, the following thermal dynamics can be observed: heating rate: the system demonstrated an extremely rapid heating rate. The samples were heated from residual temperatures (e.g., 100–200 °C) to over 800 °C in approximately 10–15 s, which corresponds to an average heating rate of over 50–60 °C/s, characteristic of solar thermal shock conditions.

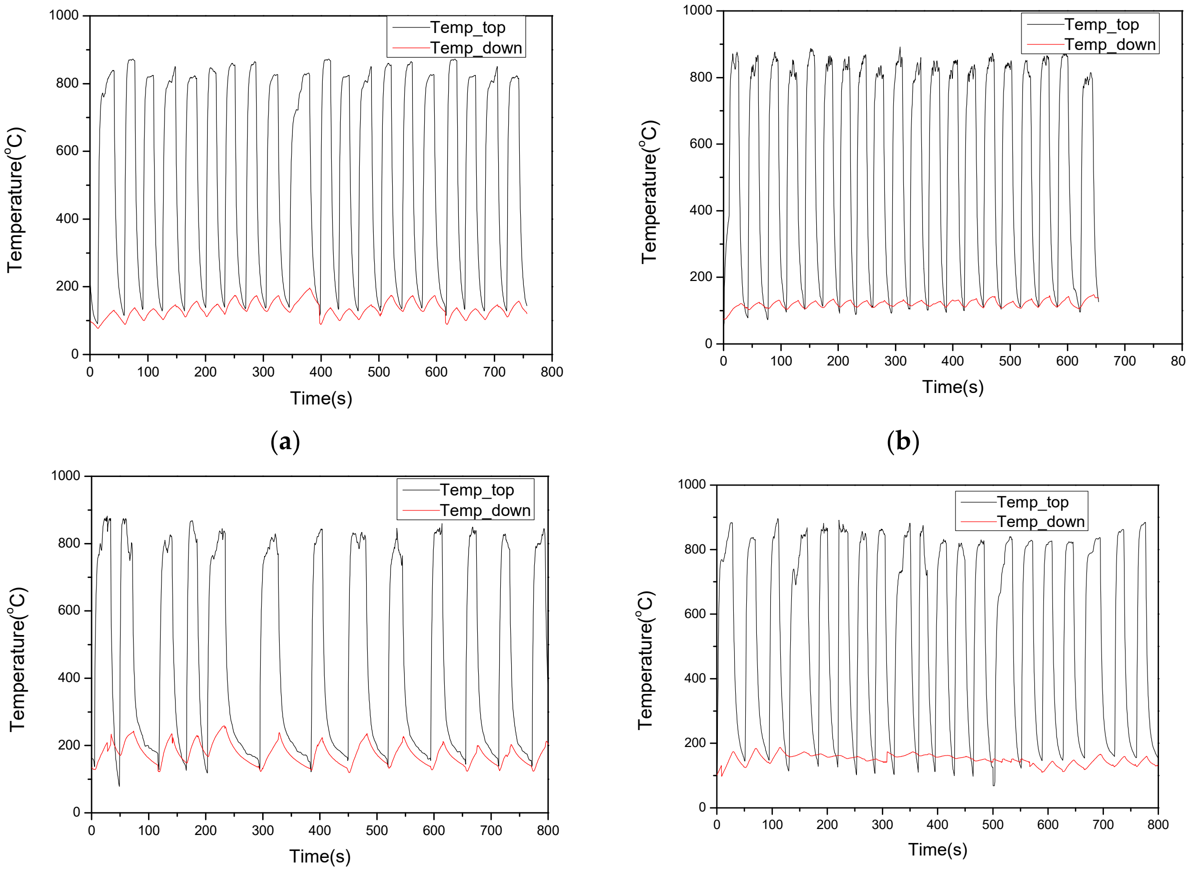

(**a**) (**b**)

(**c**) (**d**)

Figure 7. Temperature variation on the surface (black line) and under the sample (red line) for (**a**) initial sample, (**b**) S1, (**c**) S2 and (**d**) S3.

4. Discussion

The application of Metco coatings results in a visible noble shift in the surface potential, with all Ecorr values shifting towards more positive regions. A notable feature is observed in Sample 1 (Metco 71NS), which exhibits the most noble potential at −453 mV. This positive shift of over 450 mV relative to the original steel suggests that the tungsten carbide matrix fundamentally alters the interface, significantly reducing the thermodynamic affinity for corrosion reactions. While Sample 3 (Metco 45C-NS) follows a similar trend, exhibiting a potential of −570 mV, the behaviour of Sample 2 (Metco 136F) is the most interesting from an electrochemical standpoint. Although Sample 2 exhibits an Ecorr of −737 mV—less 'noble' than Samples 1 and 3—this must be correlated with the low corrosion current density (j_{corr} = 0.0045 mA/cm^2). This apparent discrepancy is typical of dense ceramic layers: while the potential is not the highest, the stability of the Cr_2O_3-SiO_2-TiO_3 film creates a kinetic barrier [27,28]. The nearly two-order-of-magnitude reduction in current density compared to the bare steel aligns with the 'stepwise' barrier protection mechanism proposed by Zhong et al. (2026) [27], where the synergistic addition of TiO_2 and SiO_2 effectively seals the inter-lamellar porosity. While these values are an improvement on the Initial sample, their performance is limited by their metallic or cermet nature. In the case of Sample 1 (Metco 71NS), the cobalt phase present between the tungsten carbide particles can generate galvanic couples on a microscopic scale, promoting the localised dissolution of the binder [29,30]. At the same time, the R_p value (polarisation resistance), as confirmed in Table 2, supports this hierarchy: Sample 2 exhibits the highest resistance (2 810 ohm·cm^2), indicating maximum resistance to charge transfer. This is in contrast to the reference steel, which has a value of only 119.51 ohm·cm^2. Regarding changes in the anodic and cathodic slopes, it can be seen that Metco coatings influence both branches of the electrochemical process. This suggests that the coatings act as mixed-type inhibitors, reducing both the rate of anodic metal dissolution and the rate of the cathodic reduction reaction (typically, oxygen reduction in aqueous media) [31].

Although it does not exhibit the highest potential, the green curve is positioned furthest to the left on the graph. The anodic slope of this sample is noticeably more abrupt than that of the control sample. This indicates that the ceramic layer (Metco 136F) covers the surface and substantially increases the activation energy required for metal ions to leave the lattice, thereby blocking the active surfaces. The clearly defined linear regions of the slopes for the coated samples suggest that, at this initial stage, the corrosion process is controlled by charge transfer at the interface rather than diffusion. However, the significant difference in performance between the initial curve and the other three samples highlights the effectiveness of the thermal spraying process in creating a controlled porous structure that is capable of isolating the substrate from the aggressive environment. The electrochemical response recorded by cyclic voltammetry establishes a link between impedance parameters and the observed surface degradation patterns. As can be seen in Figure 2b, the initial sample exhibits a higher current density than the coated samples. For the coated samples, the nearly linear profile with negligible hysteresis quantifies the transition from an active dissolution regime to a state of nearly ideal dielectric barrier. For Sample 2 ceramic coating, the anodic slope is minimal, effectively isolating the steel substrate from chloride-induced infiltration. In contrast, the high current densities recorded for Sample 1 reflect the "selective leaching of the binder" mechanism; the electrochemical consumption of the cobalt matrix increases the electrochemically active area, thereby compromising the long-term integrity of the cermet. For Sample 3, the delayed onset of current confirms the presence of an unstable passivation layer that does not match the level of robust physical barrier provided by the ceramic matrix.

Electrochemical impedance spectroscopy (EIS) analysis was performed to understand the complex mechanisms at the layer-electrolyte interface. This provided a more detailed insight into the barrier properties. The Nyquist plots obtained for the four experimental samples reveal the presence of capacitive arcs whose diameter varies significantly depending on the deposited material's nature. For the control sample (Initial), the impedance semicircle is small, which is correlated with low charge transfer resistance (R_{ct}), confirming the vulnerability of steel in a saline environment. In contrast, the impedance spectra for the coated samples indicate considerable expansion of the capacitive arc diameter, suggesting robust resistance to ionic flow. Sample 2 (Metco 136F) is clearly distinguished by a greater impedance arc, reflecting a polarization resistance value that exceeds that of the initial substrate by orders of magnitude. This trend is also confirmed by the Bode plots, in which the impedance modulus (Z) of the ceramic layer remains highest in the low-frequency range, indicating structural integrity capable of limiting electrolyte diffusion through the layer's pores. The Bode plots confirm the previously established hierarchy of anticorrosive performance and highlight the major structural differences between the four systems studied. In the impedance modulus plot (Z vs. frequency), the value obtained at low frequencies (0.01 Hz) is considered a direct indicator of the system's overall corrosion resistance. For the initial sample, the low-frequency impedance is minimal (approximately 300 Ω/cm^2), reflecting an active, unprotected surface. By contrast, Sample 2 exhibits the highest $|Z|$ value, reaching almost 10^4 Ω/cm^2, which indicates a dielectric barrier that limits ionic transfer between the electrolyte and the substrate. Phase angle analysis provides information on the quality of the protective coating. Sample 2 exhibits the widest and longest-lasting 'plateau' in phase angle, reaching a maximum value of almost 70° over a broad frequency range. This curve shape is typical of dense layers with pronounced capacitive properties, indicating that the ceramic coating (Metco 136F) behaves like an almost ideal capacitor with minimal porosity to prevent solution penetration. In the initial sample, although a phase peak is exhibited at medium frequencies, it is very narrow. This indicates a rapid relaxation of the electrochemical processes at the interface, which is characteristic of an active corrosion process. In the initial sample, although a phase peak is exhibited at medium frequencies, it is very narrow. This indicates a rapid rate of change in the electrochemical processes at the interface, which is characteristic of an active corrosion process. Samples 1 and 3 exhibit much lower phase angles (between 20 and 30), indicating behavior that is more resistive than capacitive. The low phase angle values at medium frequencies suggest the presence of structural defects or open porosity in the Co alloy layers, allowing the electrolyte to interact more easily with the metallic phases in the deposit. According to Moghanian et al. (2025) [29], such low phase angle values in the medium-frequency range are characteristic of coatings with interconnected porosity or micro-structural defects, which facilitate the rapid infiltration of Cl ions. This resistive shift suggests that the electrolyte has effectively bypassed the physical barrier, interacting directly with the metallic phases (Co binder in Sample 1 and the Co-Cr matrix in Sample 3). Similarly, Yu et al. (2024) [30] highlighted that in Cobalt-based alloys, the presence of heterogeneous grain boundaries can act as preferential paths for localized corrosion, a phenomenon that aligns with the phase angle depression observed in our EIS spectra.

The combined analysis of electrochemical and microstructural results allows the identification of a coherent degradation–protection mechanism for the investigated coating systems. The corrosion resistance of the coatings is primarily governed by their microstructural characteristics, particularly porosity, phase distribution and interlamellar cohesion, which directly influence electrolyte penetration and charge transfer processes. In the case of Sample 2 (Cr_2O_3–SiO_2–TiO_2), the dense ceramic structure with low porosity acts as an effective physical barrier, significantly limiting ionic transport toward the substrate, in correlation with values recently reported for similar Cr_2O_3-based protective systems. For instance, Mercier et al. (2025) [28] observed that even advanced Cr_2O_3 thin layers achieved through Atomic Layer Deposition exhibited lower impedance values in saline environments, highlighting the effectiveness of the APS-deposited ceramic matrix in this study.

Sample 2, Cr_2O_3–SiO_2–TiO_2, exhibits an inert ceramic barrier behaviour, which is the determining factor in its corrosion mechanism; see Figure 8. As the constituent oxides (Cr_2O_3, SiO_2, TiO_2) are already in their maximum oxidation states, the coating matrix is thermodynamically stable in a saline environment. This inherent chemical inertness prevents the matrix from participating directly in redox reactions within the investigated potential range. Consequently, the protection mechanism is purely physical and dielectric. Corrosion is localised exclusively at the base of inevitable microscopic pores (coating defects), where the electrolyte comes into contact with the steel substrate. However, the corrosion rate is limited by the impedance of the ceramic layer, which stops both ionic and electronic transport at the interface. This behaviour is confirmed by the high charge transfer resistance (Rct) and low capacitance values obtained from EIS analysis, indicating a reduced electrochemically active area. At the same time, the thermal profiles reveal the development of a pronounced temperature gradient across the coating–substrate system, suggesting reduced thermal diffusivity and an enhanced ability to attenuate thermal flux. This dual effect—blocking both ionic diffusion and thermal transfer—contributes to the stability of the coating under combined thermal and corrosive loading conditions.

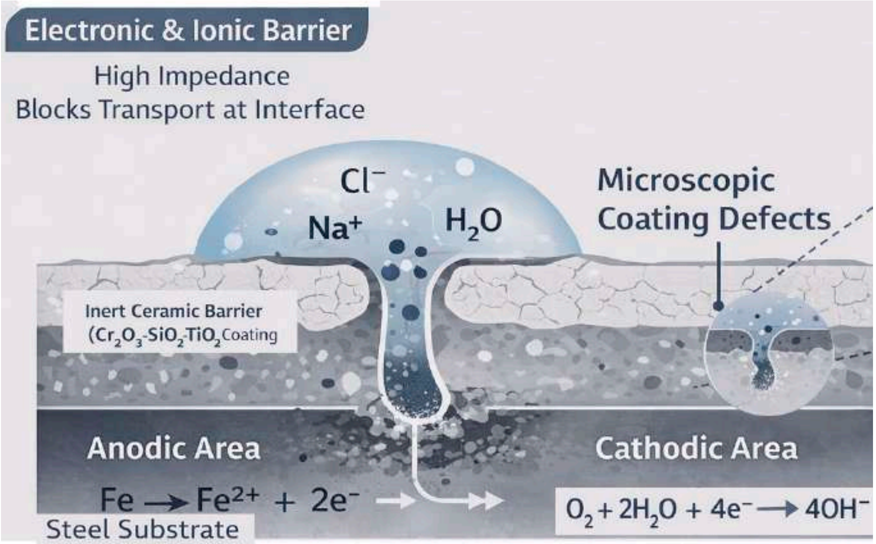

Figure 8. Corrosion mechanism of Sample 2 (Cr_2O_3–SiO_2–TiO_2).

By contrast, Sample 1 (WC/W_2C–Co) exhibits a heterogeneous microstructure in which the metallic cobalt binder forms preferential pathways for electrolyte penetration. Under corrosive conditions, this leads to selective binder dissolution, increasing the effective surface area exposed to electrochemical reactions. Although the carbide phase provides mechanical protection, the presence of interconnected microporosity reduces the barrier efficiency, as reflected by intermediate impedance values. From a thermal perspective, the reduced temperature gradient compared to the ceramic system suggests higher thermal conductivity, facilitating heat transfer towards the substrate and potentially enhancing thermally induced stresses at the interface. Similarly, Sample 3 (Co–Cr–Ni-based alloy) relies on passivation mechanisms rather than purely physical barrier effects. While chromium and nickel contribute to the formation of protective oxide films, the electrochemical results indicate that these layers are less stable and more susceptible to localised breakdown. The degradation of Sample 1 via selective binder leaching is consistent with the findings of Moghanian et al. (2025) [29]. Their research on optimized HVOF tungsten carbide coatings similarly identified the cobalt matrix as the primary electrochemical weakness; however, the higher corrosion rates observed in our APS-deposited cermet suggest that the increased micro-porosity inherent to the plasma spray process accelerates electrolyte infiltration. This correlation between increased j_{corr} and SEM-documented pitting confirms that without the thermodynamic stability of a ceramic matrix, metallic binders remain susceptible to aggressive chloride attack, regardless of the hardness of the reinforced carbide phase. The thermal response of this coating shows behaviour intermediate between metallic and ceramic systems, with limited capacity to buffer thermal gradients, which may further contribute to the instability of the passive layer under cyclic thermal loading.

Overall, the results demonstrate that optimal performance under combined thermal shock and corrosion conditions is achieved by coatings that simultaneously minimise porosity, limit electrolyte access, and reduce thermal diffusivity, thereby ensuring both chemical and thermomechanical stability.

Analysis of the cooling rate for air cooling (natural cooling) shows a gradual decrease in temperature immediately after removal from the solar focus. In the first 5 s after the flow ceases, the temperature typically drops by approximately 300–400 °C (e.g., from 850 °C to 500 °C). In the case of forced cooling in cycles where compressed air was applied, the cooling rate is much steeper, ensuring the rapid temperature drop required to test the adhesion of the ceramic layer under sudden contraction [32]. A comparative analysis of the thermal profiles presented in Figure 7 reveals distinct differences in the temperature evolution between the uncoated substrate and the coated systems. In the case of the initial sample (Figure 7a), the temperature curves recorded at the surface and within the substrate exhibit a relatively close overlap throughout the heating and cooling stages, indicating efficient heat transfer and the absence of any thermal gradient buffering. This behaviour reflects the direct exposure of the metallic substrate to the thermal flux, resulting in rapid heat penetration and a more uniform temperature distribution across the sample thickness. In contrast, the coated samples (Figure 7b–d) display a more pronounced separation between the surface and subsurface temperature curves, particularly during transient heating and cooling stages. This divergence suggests the development of a temperature gradient across the coating–substrate system, associated with the reduced thermal diffusivity of the deposited layers. The effect is most evident in the ceramic coating (Sample 2), where the delay between surface heating and substrate response is more significant, indicating enhanced thermal insulation capacity [33].

Additionally, the coated systems exhibit a smoother temperature transition at the substrate level, with attenuated fluctuations compared to the uncoated sample. This behaviour implies that the coatings act not only as thermal barriers but also as stabilizing layers that mitigate abrupt thermal variations transmitted to the substrate. Such damping of thermal gradients is essential for reducing thermally induced stresses at the interface, thereby contributing to improved structural integrity under cyclic thermal loading conditions [34]. In conclusion, based on visual inspection following testing at 800 °C, no delamination, macroscopic cracks, or damage to the ceramic coatings (Metco 71NS, Metco 136F, Metco 45C-NS) was observed. This suggests good thermomechanical compatibility between the steel substrate and the deposited layers, despite the high rates of temperature variation [35].

Despite the relevant insights provided by this study, several limitations should be acknowledged. First, the corrosion behaviour was evaluated in a simplified laboratory environment (0.9% NaCl solution), which does not fully replicate the complex chemical composition of natural soils, where multiple ionic species and pH variations may influence degradation mechanisms. Second, the thermal shock tests were conducted under controlled single-cycle conditions, without considering long-term cyclic loading, which may lead to cumulative damage such as fatigue-induced microcracking or progressive delamination.

In addition, although microstructural observations after corrosion testing confirm the integrity of the coatings, a detailed quantitative analysis of defect evolution (e.g., crack density, porosity variation after thermal shock) was not performed. Furthermore, the study focuses primarily on corrosion and thermal behaviour, without addressing tribological performance, which is a critical factor for agricultural applications.

Future work should therefore consider multi-cycle thermal shock testing, combined corrosion–wear experiments, and more detailed quantitative microstructural characterization in order to provide a comprehensive assessment of coating durability under real service conditions.

5. Conclusions

This study provides a systematic evaluation of the anticorrosive performance of various thermally sprayed Metco coatings on carbon steel in a 0.9% NaCl environment. The experimental findings led to the following conclusions:

- Electrochemical efficiency: The ceramic coating (Sample 2) provided the greatest level of protection. It exhibited a significant shift in corrosion potential (Ecorr) towards more noble values, reducing the corrosion rate by almost two orders of magnitude compared to the bare substrate.

- Interfacial stability: EIS modelling revealed that, whereas Samples 1 and 3 rely on sacrificial or passive mechanisms, Sample 2 acts as a near-ideal dielectric barrier. The high R (ct) values (2213 $\Omega\cdot cm^2$) and low double-layer capacitance (C) confirm a significant reduction in the electrochemically active area at the substrate base.
- Microstructural degradation: Post-corrosion SEM analysis revealed a shift from severe uniform oxidation of the steel substrate to selective binder leaching in the Co-based coatings. In contrast, the Cr_2O_3-based ceramic matrix remained structurally intact, proving its superior chemical inertness against chloride ion attack.
- Industrial applicability: The combination of physical barrier effects and interfacial resistance makes the Cr_2O_3-4SiO_2-3TiO system the optimal solution for the long-term protection of structural steel in aggressive saline environments.

Author Contributions: Conceptualization, C.M. and R.C.; methodology, B.I.; software, R.C.; validation, B.I., F.-C.L. and I.M.; formal analysis, V.V.; investigation, B.N.; resources, I.M.; data curation, V.V.; writing—original draft preparation, R.C.; writing—review and editing, F.-C.L.; visualization, B.N.; supervision, C.M.; project administration, C.M.; funding acquisition, I.M. All authors have read and agreed to the published version of the manuscript.

Funding: This work was supported by a grant from the Ministry of Research, Innovation and Digitization, CNCS-UEFISCDI, project number PN-IV-P8-8.3-ROMD-2023-0108, within PNCDI IV.

Institutional Review Board Statement: Not applicable.

Informed Consent Statement: Not applicable.

Data Availability Statement: The original contributions presented in this study are included in the article. Further inquiries can be directed to the corresponding author.

Acknowledgments: The authors would like to express their gratitude to the Processes, Materials and Solar Energy Laboratory (PROMES-CNRS), Font-Romeu, France, for providing the facilities and technical support necessary to conduct this research.

Conflicts of Interest: The authors declare no conflicts of interest.

References

1. Dinesh, K.V.; Sivasubramanian, M.; Vairavel, M. Enhanced corrosion resistance of copper for agricultural equipment using superhydrophobic stearic acid coatings. *Materia* **2025**, *30*, e20240647. [CrossRef]
2. Jun, H.; Shijun, H.; Zhen, W.; Jianbo, Z.; Liping, W.; Zhong, C. Stearic acid-coated superhydrophobic Fe_2O_3/Fe_3O_4 composite film on N80 steel for corrosion protection. *Surf. Coat. Technol.* **2019**, *359*, 47–54. [CrossRef]
3. Munteanu, C.; Melnic, I.; Istrate, B.; Hardiman, M.; Gaiginschi, L.; Lupu, F.C.; Arsenoaia, V.N.; Chicet, D.L.; Zirnescu, C.; Badiul, V. A comprehensive review of improving the durability properties of agricultural harrow discs by atmospheric plasma spraying (APS). *Coatings* **2025**, *15*, 632. [CrossRef]
4. Monika, M.; Pawel, S.; Mirosław, S.; Mariusz, W.; Leszek, L.; Toma, F.L.; Stefan, B. Wear Behavior Analysis of Al_2O_3 Coatings Manufactured by APS and HVOF Spraying Processes Using Powder and Suspension Feedstocks. *Coatings* **2021**, *11*, 879. [CrossRef]
5. Shivam, P.; Anuj, B.; Ankita, O.; Anil, K.S.; Deepak, K.G.; Jagtar, S.; Munish, K.G. Effect of fuel pressure, feed rate, and spray distance on cavitation erosion of Rodojet sprayed Al_2O_3+50%TiO_2 coated AISI410 steel. *Surf. Coat. Technol.* **2021**, *410*, 126961. [CrossRef]
6. Szala, M.; Dudek, A.; Maruszczyk, A.; Walczak, M.; Chmiel, J.; Kowal, M. Effect of Atmospheric Plasma Sprayed TiO_2–10% NiAl Cermet Coating Thickness on Cavitation Erosion, Sliding and Abrasive Wear Resistance. *Acta Phys. Pol. A* **2019**, *136*, 335–341. [CrossRef]
7. Mervi, S.; Tommi, V.; Maria, O.; Tomi, S.; Petri, V. Comparative Study on the Corrosion Performance of APS-, HVOF-, and HVAF-Sprayed NiCr and NiCrBSi Coatings in NaCl Solutions. *J. Therm. Spray Technol.* **2022**, *31*, 1581–1597. [CrossRef]
8. Sadeghimeresht, E.; Markocsan, N.; Nylén, P. Microstructural and Electrochemical Characterization of Ni-Based Bi Layer Coatings Produced by the HVAF Process. *Surf. Coat. Technol.* **2016**, *304*, 606–619. [CrossRef]
9. Papageorgiou, N.; Bonin, A.; Espallargas, N. Tribocorrosion mechanisms of NiCrMo-625 alloy: An electrochemical modeling approach. *Tribol. Int.* **2014**, *73*, 177–186. [CrossRef]

10. Ding, P.; Cai, T.; Sun, J.; Ma, L.; Zheng, X.; Chen, H. Delamination mechanism and assessment of thermal barrier coating system under thermal cycling. *Case Stud. Therm. Eng.* **2025**, *74*, 106726. [CrossRef]
11. Xiong, Y.; Shujuan, D.; Jinyan, Z.; Xin, Z.; Jianing, J.; Longhui, D.; Xueqiang, C. Sliding wear characteristics of plasma sprayed Cr_2O_3 coatings with incorporation of metals and ceramics. *Ceram. Int.* **2019**, *45*, 20243–20250. [CrossRef]
12. Medabalimi, S.; Ramesh, M.; Kadoli, R. High-Temperature Solid Particle Erosion Behavior of Partially Oxidized NiCrBSiFe/NiCr Plasma Spray Coatings. *J. Therm. Spray Technol.* **2021**, *30*, 1638–1652. [CrossRef]
13. Kalácska, Á.; De Baets, P.; Fauconnier, D.; Schramm, F.; Frerichs, L.; Sukumaran, J. Abrasive wear behaviour of 27MnB5 steel used in agricultural tines. *Wear* **2020**, *442–443*, 203107. [CrossRef]
14. Arsenoaia, V.N.; Munteanu, C.; Lupu, F.C.; Istrate, B.; Benchea, M.; Melnic, I. Field Performance and Wear Behavior of Atmospheric Plasma Spraying (APS) Coated Discs Used in Agricultural Disc Harrows. *Agriculture* **2026**, *16*, 114. [CrossRef]
15. Lakkannavar, V.; Yogesha, K.B.; Durga Prasad, C.; Phanden, R.K.; Srinivasa, G.; Chandrashekar Prasad, S. Thermal spray coatings on high-temperature oxidation and corrosion applications—A comprehensive review. *Results Surf. Interfaces* **2024**, *16*, 100250. [CrossRef]
16. Li, H.; Feng, X.; Wang, X.; Yang, X.; Tang, J.; Gong, J. Impact of temperature on corrosion behavior of austenitic stainless steels in solar salt for CSP application: An electrochemical study. *Sol. Energy Mater. Sol. Cells* **2022**, *239*, 111661. [CrossRef]
17. Bolat, G.; Mareci, D.; Iacoban, S.; Cimpoesu, N.; Munteanu, C. The Estimation of Corrosion Behavior of NiTi and NiTiNb Alloys Using Dynamic Electrochemical Impedance Spectroscopy. *J. Spectrosc.* **2012**, *2013*, 714920. [CrossRef]
18. Izquierdo, J.; Bolat, G.; Cimpoesu, N.; Trinca, L.C.; Mareci, D.; Souto, R.M. Electrochemical characterization of pulsed layer deposited hydroxyapatite-zirconia layers on Ti-21Nb-15Ta-6Zr alloy for biomedical application. *Appl. Surf. Sci.* **2016**, *385*, 368–378. [CrossRef]
19. Darabont, D.-C.; Moraru, R.I.; Antonov, A.E.; Bejinariu, C. Managing new and emerging risks in the context of ISO 45001 standard. *Qual.-Access Success* **2017**, *18*, 11–14.
20. Popov, B.N. (Ed.) Basics of Corrosion Measurements. In *Corrosion Engineering*, 2nd ed.; Elsevier: Oxford, UK, 2025; pp. 187–244. [CrossRef]
21. Lgaz, H.; Lee, H.-S.; Messali, M. Self-healing ceramic coatings: Mechanisms, design strategies, and emerging applications for extreme environments. *Ceram. Int.* **2025**, *51*, 54423–54470. [CrossRef]
22. Yao, Z.; Jiang, Z.; Wang, F. Study on corrosion resistance and roughness of micro-plasma oxidation ceramic coatings on Ti alloy by EIS technique. *Electrochim. Acta* **2007**, *52*, 4539–4546. [CrossRef]
23. Zhao, J.; Fan, W.; Liu, W.; Liang, Q.; Chen, P.; Cheng, Y. Investigation into enhanced electrochemical hydrogen storage performance of Co0.9Cu0.1Si alloy via cobalt–nitrogen co-doped reduced graphene oxide coating. *J. Phys. Chem. Solids* **2026**, *211*, 113459. [CrossRef]
24. Ma, J.; Kong, G.; Wang, K.; Liu, Z.; Zhao, L.; Yang, H.; Liu, C.; Tian, A.; Wang, Y. Corrosion−creep behavior of high−chromium nickel-based superalloys in the accelerated marine-atmospheric environment. *Eng. Fail. Anal.* **2025**, *182*, 110091. [CrossRef]
25. Ahmed, S.; Hou, Y.; Lepkova, K.; Pojtanabuntoeng, T. Investigation of the Effect Chloride Ions on Carbon Steel in Closed Environments at Different Temperatures. *Corros. Mater. Degrad.* **2023**, *4*, 364–381. [CrossRef]
26. Li, J.; Lu, K.; Zhang, Z.; Liu, H.; Li, D.; Tan, D. Overview of the impact of nickel-based catalyst on corrosion mechanism for steel. *J. Environ. Chem. Eng.* **2024**, *12*, 114552. [CrossRef]
27. Zhong, Q.; Ran, C.; Chen, Z.; Dong, X.; Zeng, Z.; Luo, X.; Li, W.; Na, J.; Wang, L.; Ye, J. Electrochemically enhanced uniform TiO_2 films on TA1 titanium via stepwise anodizing: Decoupling grain-orientation effects and corrosion-resistance mechanisms. *Surf. Coat. Technol.* **2026**, *523*, 133120. [CrossRef]
28. Mercier, D.; Zazpe, R.; Wang, X.; Michaux, M.; Rodriguez-Pereira, J.; Zanna, S.; Seyeux, A.; Macak, J.M.; Marcus, P. Enhanced corrosion resistance of 2024 aluminum alloys with Cr_2O_3 thin layers by Atomic Layer Deposition. *Corros. Sci.* **2025**, *256*, 113167. [CrossRef]
29. Moghanian, A.; Mohammadi, M.A.; Ansari, J.; Asadi, P.; Akbari, M.; Yazdi, M.S.; Safaee, S. Enhancing corrosion resistance of AISI 4130 steel through optimized HVOF tungsten carbide coatings. *Results Surf. Interfaces* **2025**, *18*, 100450. [CrossRef]
30. Yu, Q.; Zhang, W.; Shang, J.; Liu, B.; Pei, Y.; Li, Y.; Ao, S. Comparative investigation on the microstructure and corrosion properties of surfacing cobalt alloys by various methods. *Surf. Coat. Technol.* **2024**, *494*, 131386. [CrossRef]
31. Cimpoesu, N.; Trinca, L.C.; Dascalu, G.; Stanciu, S.; Gurlui, S.O.; Mareci, D. Electrochemical Characterization of a New Biodegradable FeMnSi Alloy Coated with Hydroxyapatite-Zirconia by PLD Technique. *J. Chem.* **2016**, *2016*, 9520972. [CrossRef]
32. Ashofteha, A.; Mashhadia, M.M.; Amadehb, A.; Seifollahpour, S. Effect of layer thickness on thermal shock behavior in double-layer micro- and nano-structured ceramic top coat APS TBCs. *Ceram. Int.* **2017**, *43*, 13547–13559. [CrossRef]
33. Abedi, H.R.; Salehi, M.; Shafyei, A. Microstructural, mechanical and thermal shock properties of triple-layer TBCs with different thicknesses of bond coat and ceramic top coat deposited onto polyimide matrix composite. *Ceram. Int.* **2018**, *44*, 6212–6222. [CrossRef]

34. Gilbert, A.; Kokini, K.; Sankarasubramanian, S. Thermal fracture of zirconia–mullite composite thermal barrier coatings under thermal shock: An experimental study. *Surf. Coat. Technol.* **2008**, *202*, 2152–2161. [CrossRef]
35. Liang, L.H.; Li, X.H.; Chen, L.F.; Wei, Y.G. Effect of ceramic coating thickness on fracture behaviour of coating structure under thermal shock cycles. *Ceram. Int.* **2022**, *48*, 11435–11444. [CrossRef]

https://doi.org/10.3390/app16083703